MDPI

Article

Calibrating A Hybrid Smoke Plume Model from Ground-Based Imagery with Levenberg-Marquardt

Gene Huntley, Stephen Guerin, Kasra Manavi, Joshua Thorp, Jaime Gould, and Stephen Graydon [2,*]

[1] V Sue Cleveland High School; CHS@rrps.net
[2] SimTable; sales@simtable.com
* Correspondence: e-mail@e-mail.com; Tel.: (optional; include country code; if there are multiple corresponding authors, add author initials) +xx-xxxx-xxx-xxxx (F.L.)
† Current address: Affiliation.
‡ These authors contributed equally to this work.

Abstract: Smoke plumes pose one of the largest threats in wildfire emergencies due to their capacity to carry embers and particulate matter over large distances. However, they can also be crucial in fighting wildfires due to their capability to provide information on wildfire parameters from vegetation to fire intensity, emphasizing the importance of having 3-dimensional models and predictions of smoke plumes. Previous studies have established methods to simulate these smoke plumes, but have encountered real-world limited accuracy due to a lack of information on input vectors such as wind or temperature, which significantly impact plume prediction accuracy. This study addresses these limitations by matching forecasts of smoke plume with observed imagery through optimizing input vectors. First, smoke plumes are generated with the Navier-Stokes equations based on historical fire perimeters with known weather vectors, and Levenberg-Marquardt is run to fit the simulated smoke plume to the calibrated imagery by fine-tuning the input vectors. Such an optimization of the smoke plume model promises not only an increased accuracy of smoke plume prediction, but also provides crucial information on weather vectors that allows for other forms of forecast.

Keywords: smoke; photogrammetry; optimization; imagery; simulations; wildfires

1. Introduction

Wildfires have increased in frequency and intensity, creating greater smoke plume emissions, leading to the degradation of global atmospheric quality [1]. This increase in emissions poses a critical public health issue, as wildfire emissions contain particulates like PM2.5 that are associated with cardiovascular and respiratory illnesses [2–5], attributable to 339,000 deaths annually [7]. In addition, due to the indoor restrictions poor air quality may impose, wildfire emissions have caused a significant decrease in civilian mental health [6]. Finally, wildfire smoke emissions also serve as both a precursor for O_3 emissions and aerosol light absorbance in the atmosphere [8]. Given the significant atmospheric and public health implications posed by smoke plume emission, understanding their emission and composition through construction of said smoke plume poses a relevant problem.

The predominant way to construct smoke plumes is through physical models which take meteorological and geographical factors - e.g. elevation, temperature, humidity - as input [10–13]. Given the limited granularity of certain input vectors, especially the spatial and temporal resolution of wind speeds at different elevations [13,14], smoke plumes may experience limited accuracy during simulation. Parameter-space exploration of computational fluid dynamics (CFD) based smoke plume and cloud simulations show that large relative variations of input vectors can greatly alter the composition of the geometry of smoke plumes [15,16], emphasizing the necessity of precise atmospheric data in these simulations.

Satellite images of smoke plumes - automatically identified and segmented in surveillance footage [17–19] - have frequently been used to verify the aforementioned physical

Citation: Lastname, F.; Lastname, F.; Lastname, F. Title. *Fire* **2024**, *1*, 0. https://doi.org/

Received:
Revised:
Accepted:
Published:

models [11,12]. HYSPLIT - NOAA's smoke emission model - utilizes this abundance of smoke plume satellite segmentation data to fine-tune smoke plume emission locations by minimizing the error between observed imagery and predicted values [20]. While computationally efficient and accurate, the optimization poses two problems: (1) the study does not provide methodology to optimize parameters outside location and (2) limited spatial and/or temporal resolution of satellite imagery [21,22], the study focuses on smoke plumes spanning a large geographic region. Since ground-based imagery - like cellphones and mounted cameras - that are capable of multi-media recording are ubiquitous [23,24], this study attempts to remediate both problems by (1) creating a framework that allows other meteorological parameters like wind speed and temperature to be optimized and (2) utilizing ground-based imagery as the basis for optimization rather than satellite imagery.

The study first provides a hybrid Lagrangian-Eulerian computational fluid dynamic model evaluated on preliminary guesses of meteorological information taken from nearby weather stations. Then, Levenberg-Marquardt - a variant of gradient descent - reduces the difference between predicted simulations and observed ground-based imagery by approximating derivatives with respect to a defined error function. The effectiveness of such optimizations is tested on two metrics: (1) the difference between observed and predicted imagery and (2) the ability for the algorithm to converge onto crucial smoke plume parameters. Given the abundance of mounted cameras in California in the form of a surveillance database ALERTCalifornia [24], this study's scope will primarily be concentrated in the Western coast of the United States.

We will present the remaining content of this paper as follows: Section 2 will present the equations necessary to simulate and optimize the smoke plume and an algorithm to utilize the aforementioned equations. In Section 3, the accuracy of the algorithm evaluated on 7 wildfire incidents and its optimal use cases will be presented. Lastly, Section 4 contains the conclusion.

2. Materials and Methods

2.1. Fluid Dynamics Simulation

When a fuel cell undergoes combustion, it rapidly loses mass. The mass in a particular area in a discretized grid can be defined as $m : (x, y, z, t) \rightarrow s$, where s is a scalar value. Given information about fuel and vapor content, the mass loss of a fuel cell (m'), the heat of combustion (ΔH), and the rate of heat release (Q') can be represented as

$$\Delta H = \frac{Q'}{m'} \tag{1}$$

for each fuel cell undergoing combustion. From Rothermel's fire spread model [25], for a cell $m(x, y, z)$ that is going through combustion,

$$\frac{dm}{dt} = \Gamma' m_0 \eta_m \eta_s \tag{2}$$

$$= 0.417\Gamma' m_0 [1 - 2.59(\frac{q_v}{M_x}) + 5.11(\frac{q_v}{M_x})^2 - 3.52(\frac{q_v}{M_x})^3] \tag{3}$$

$$\Gamma' = \Gamma'_{\max}(\frac{\beta}{\beta_{opt}})^A \exp[A(1 - \frac{\beta}{\beta_{opt}})] \tag{4}$$

$$\beta_{opt} = 3.348\sigma^{-0.8189} \tag{5}$$

$$A = 133\sigma^{-0.77913} \tag{6}$$

$$\beta = \frac{m_0}{32\delta} \tag{7}$$

where σ is surface area to volume ratio ($\frac{1}{m}$), m_0 represents the initial fuel bed mass ($\frac{\text{kg}}{\text{m}^2}$), δ is the fuel bed depth (m), and q_v a dimensionless ratio of atmospheric vapor content (defined more formally later in the section), all of which are defined value for every discretized cell. Otherwise, if a fuel cell isn't undergoing combustion, $\frac{dm}{dt} = 0$.

We can also account for the smoke plume emission with respect to both the evaporation and mass loss. The smoke plume scalar field, defined as $q_s : (x, y, z, t) \rightarrow q_s(x, y, z, t)$, can be calculated as

$$\frac{\partial q_s}{\partial t} + u \cdot \nabla q_s = -\frac{dm}{dt}(s_M + s_W c_{WM}) \tag{8}$$

as shown by [13]. For each smoke scalar value s in the discretized grid q_s, $\lfloor s \rfloor$ points is generated in each location, where the set of all smoke plume points are defined as Q_s.

Next, given the rate of mass fuel loss, the module temperature of each fuel cell - defined as $T_M : (x, y, z, t) \rightarrow T_M(x, y, z, t)$ - can computed. Therefore, from the equations provided in [13], the combustion heat of each discretized cell can be derived as

$$S(x) = \frac{x}{x + 0.7(1 - x)} \tag{9}$$

$$\mu(u) = (\mu_{max} - 1)/S(u/u_{ref}) - 1 \tag{10}$$

$$T_M = (T_1 - T_0)S^{-1}(\frac{[\frac{dm}{dt}]}{\mu(u)cA}) + T_0 \tag{11}$$

where $T_0 = 150°\text{C}$ and $T_1 = 450°\text{C}$. Note that $S(x)$ is an invertible interpolation function that transitions values $[0, 1]$ for temperatures between $[T_0, T_1]$ created solely for the purpose of this derivation.

Given the possibility of pyrocumulus clouds, clouds produced by wildfires that are highly visible in camera imagery [26], water evaporation and content needs to be taken into account. Let q_v, q_r, q_c be three discretized scalar fields defined as vapor content, rain, and condensation, respectively. More formally, $q_v : (x, y, z, t) \rightarrow q_v(x, y, z, t)$, $q_c : (x, y, z, t) \rightarrow q_c(x, y, z, t)$, and $q_r : (x, y, z, t) \rightarrow q_r(x, y, z, t)$. In that case, the change in the three scalar fields can be defined as

$$\frac{\partial q_v}{\partial t} + u \cdot \nabla q_v = -C_c + E_c + E_r + V_r \tag{12}$$

$$\frac{\partial q_r}{\partial t} + u \cdot \nabla q_r = C_c - E_c - A_c - K_c \tag{13}$$

$$\frac{\partial q_c}{\partial t} + u \cdot \nabla q_c = A_c + K_c - E_r - V_r \tag{14}$$

such that

$$E_c - C_c = \min(q_{v,sat} - q_v, q_c) \tag{15}$$

$$A_c = \beta_A \max(q_c - a_T) \tag{16}$$

$$K_c = \beta_K q_c q_r \tag{17}$$

$$E_r = q_r w \max(q_{v,sat} - q_v, 0) \tag{18}$$

where w, β_A, β_K are dimensionless evaporation, accretion, and condensation parameters [27]. For each scalar value s of q_v, q_c, q_r, $\lfloor s \rfloor$ points are created at each discretized grid cell. All the points generated by q_v, q_c, q_r are defined as Q_v, Q_c, Q_r, respectively. $q_{v,sat}$, the amount of water content an air particle can hold, is defined as

$$q_{v,sat}(T, p) = \frac{380.16}{p} \exp(\frac{17.67T}{T + 243.5}) \tag{19}$$

where T is temperature in Celsius, and p is the pressure in Pascals [16].

Finally, we can define wind as a vector-field, denoted as $u : (x, y, z, t) \rightarrow u(x, y, z, t)$. The temporal evolution of the wind field can be described by the Navier-Stokes equation such that

$$\frac{\partial u}{\partial t} + u \cdot \nabla u = \nu \nabla^2 u - \frac{1}{\rho} \nabla p + \frac{\vec{f} + \vec{B}}{\rho} \tag{20}$$

where p is a pressure field $p : (x, y, z, t) \rightarrow p(x, y, z, t)$, ν as the viscosity of wind, ρ as wind density, and $\vec{f} + \vec{B}$ as external wind vectors [28]. To enforce the incompressibility assumption of Equation 20,

$$\nabla \cdot u = 0 \tag{21}$$

is enforced, ensuring the conservation of momentum. Note that pyroculumus clouds generated by smoke plumes frequently exhibit anvil-like conditions, similar to a supercell cloud. Thus, buoyancy is defined as the following [16] such that it results in observed anvil-like formations:

$$B(\vec{z}) = g(1.607 \frac{T_{th}(z)}{T(z)}) \tag{22}$$

Finally, the thermal packet and the background temperature can be defined as

$$T(z) = T_0 + T'(\min(z, z_0)) - T'(\max(z - z_0, 0)) \tag{23}$$

$$T_{th}(z) = T(0)(\frac{p(z)}{p(0)}) \tag{24}$$

$$p(z) = (1 - 0.0065 \frac{h}{T(0)})^{5.2561} \tag{25}$$

such that T' is the temperature slope and $2z_0$ is the roof of the cloud anvil [16].

2.2. Optimization

After creating a Lagrangian-Eulerian hybrid smoke plume model, its parameters need to be optimized. Since the objective of the study is to optimize for smoke plume parameters with ground-based images, image plane $I = (R, T, I)$ needs to be defined such that $R = (\alpha, \beta, \gamma)$ (representing the pan, tilt, and roll of the camera), $T = (x, y, z)$ (representing the Earth-Centered-Earth-Fixed coordinates of the camera), and $I = (f, [p_x, p_y])$ (representing the focal point, f, and the principal point offset of the camera, p_x, p_y). A change-in-basis to convert global ECEF (Earth-Centerd-Earth-Fixed) coordinates would be done through transformation matrix M_T such that

$$\begin{aligned} \vec{u} &= \begin{bmatrix} x & y & z \end{bmatrix} \\ \vec{t} &= \vec{u} \times \begin{bmatrix} 0 & 0 & -1 \end{bmatrix} \\ \vec{r} &= \vec{u} \times \vec{t} \\ M_T &= \begin{bmatrix} \frac{\vec{f}}{|\vec{f}|} & \frac{\vec{t}}{|\vec{t}|} & \frac{\vec{u}}{|\vec{u}|} \end{bmatrix} \end{aligned}$$

For an arbitrary set of points S, the operation $\dot{S}$ on set $S = \{p_1, p_2, ..., p_n\}$ to transform set S from global ECEF coordinates to image plane coordinates is defined as

$$R_x(\alpha) = \begin{bmatrix} 1 & 0 & 0 \\ 0 & \cos(\alpha) & -\sin(\alpha) \\ 0 & \sin(\alpha) & \cos(\alpha) \end{bmatrix} \tag{26}$$

$$R_y(\beta) = \begin{bmatrix} \cos(\beta) & 0 & \sin(\beta) \\ 0 & 1 & 0 \\ -\sin(\beta) & 0 & \cos(\alpha) \end{bmatrix} \tag{27}$$

$$R_z(\gamma) = \begin{bmatrix} \cos(\gamma) & -\sin(\gamma) & 0 \\ \sin(\gamma) & \cos(\gamma) & 0 \\ 0 & 0 & 1 \end{bmatrix} \tag{28}$$

$$C(p) = \frac{\vec{p} M_T R_x(\alpha) R_y(\beta) R_z(\gamma)}{f} \tag{29}$$

$$\dot{S} = \{(\frac{C(p)_1}{C(p)_3}, \frac{C(p)_2}{C(p)_3}) | \forall p \in S\} \tag{30}$$

where $\vec{C(p)}_n = \{x, y, z\}$ denotes the nth component of vector $C(p)$.

Before any accuracy evaluation can be completed, a segmentation of the image should be performed. For the purposes of this study, the segmentation was completed manually, where a polygon containing the smoke plume from the image was cropped out as seen in Figure 1. Let the set of pixels contained in image I's segmentation be denoted as $\Omega_I = \{(x_1, y_1), (x_2, y_2), ...(x_n, y_n)\}$.

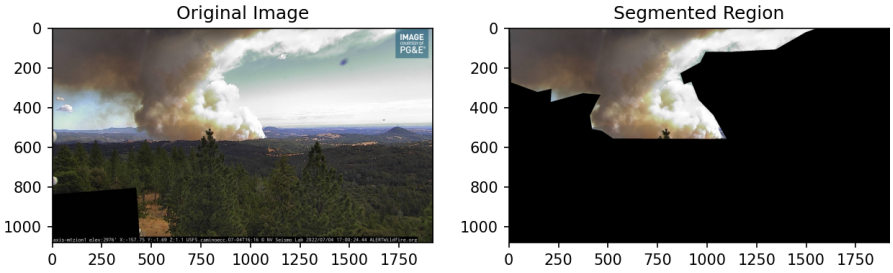

Figure 1. On the left, there is an uncropped image of a smoke plume. Note that portions of the image that display private property is blacked out. On the right is the segment of the plume being manually cropped out.

To evaluate the accuracy of the smoke plume simulation, after running the computational fluid simulation for 10 iterations on a $(15, 15, 25)$ discretized grid, each point is projected onto the camera, with their global coordinates converted to (u, v) pixel coordinates. Each point on the picture is either inside or outside the segmentation; thus, if a projected point were to fall onto a point where a pixel falls outside the segmentation or if no projected point falls onto a pixel within the segmentation, a score of 1 is added to a total T, which Levenberg-Marquardt attempts to find the global minimum for. For a set of points P, let the total score for the evaluation be defined as

$$S(P, \Omega_I) \tag{31}$$

An example is shown in Figure 2.

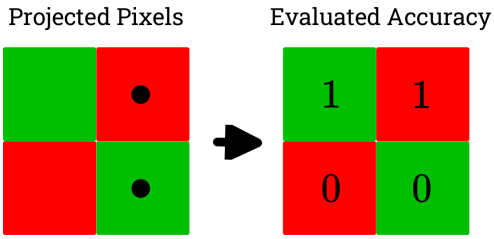

Figure 2. In the top left corner, the pixel is in the segmentation; however, no point is in the pixel. Thus, it adds a score of 1. In the top right corner, the pixel isn't in the pixel, adding a score of 1. In the bottom left corner, no point is in the non-segmented pixel and in the bottom right corner, there is a point in the segmented pixel. Thus, the total score is 2.

Since the optimization of every single discretized cell for mass/wind values would scale cubically with cell discretization values, for both the wind and mass matrices, non-negative matrix factorization (NNMF) is performed to reduce the dimensionality of each matrix to ensure a linear scaling of runtime. The algorithm approximates an original matrix M by factoring it into two other distinct, non-negative matrices.

To perform the factorization, a constant c is first selected, splitting a matrix M into c equal components, $M_1, M_2, ..., M_c$. For each component M_i, NMMF is performed to reduce $M_i = I_i \times O_i$, giving us sets

$$M' = \{I_1, I_2, ..., I_c\} \tag{32}$$

$$M'' = \bigcup_{x=1}^{c} \{O_{x,i,j} | \forall i, j \leq c\} \tag{33}$$

to be used for optimization. NMMF is performed on matrices $f_{ext,x}, f_{ext,y}, f_{ext,z}, m$.

Finally, the parameter set $\kappa = \{z_0, T'\} \cup f''_{ext,x} \cup f''_{ext,y} \cup m''$ is optimized with Levenberg-Marquadt by first defining a Jacobian matrix, such that

$$J_{i,j} = \frac{\partial S_i}{\partial \kappa} \tag{34}$$

and update each value in κ with a Levenberg-Marquardt iteration [29], defined as

$$\kappa' = -[J^T J + \lambda \text{diag}(J^T J)]^{-1} J^T S(Q_s \cup Q_c, \Omega_I) \tag{35}$$

For further clarification, algorithm A1 is provided in the Appendix for the optimization step of a single camera.

3. Results and Discussion

3.1. Simulation Design

This study was focused in California due to both the abnormal frequency of fires and the presence of an extensive surveillance network in the form of mounted cameras called ALERTCalifornia. Fire perimeters were scraped from SimTable's Fire Progressions database, which contains fire perimeter rasters with respect to time. 53 wildfires were automatically selected based on proximity to the camera network, which was then manually narrowed down to only 7 wildfires based on visibility of smoke plumes.

Initial inputs for metereological data was obtained from NOAA's National Weather Service, providing historical data for humidity, wind angle, wind intensity, and surface temperature [30]. Every value in the discretized grid - both for temperature and wind vectors - were homogeneous.

Next, fuel parameters were taken from vegetation surveys of the different wildfire burn areas. Parameters for each of the wildfires are shown in Table 1. In addition, variables were set to the following: $\beta_A = 0.2$, $\beta_K = 0.4$, $w = 0.6$, $\sigma = 3734\frac{1}{m}$, $\delta = 1m$, $c = 2$ for all the wildfires listed in the table.

Table 1. The table shows each incident simulated and the initialized parameters for each incident.

Wildfire Name [32]	Wind Direction [30]	Wind Speed (mph) [30]	Fuel Density (kg/m^2) [31]	Burn Time [32]	Surface Temp (F) [30]	Weather Station [30]
Fairview	East	15	10.418	5d 9h	70	Ontario A/P
Mosquito	South	27	7.406	45d 8h	63	Sacramento A/P
Oak	Northwest	6.7	2.323	43d 2h	93	Merced A/P
Electra	West	8.2	4.689	24d 9h	74	Stockton A/P
Summit	Northwest	8.4	2.959	9d 16h	83	Visalia A/P
Kelly	Southwest	11	12.29	26d 22h	57	Saguache A/P
Smith River	West	22	12.29	94d 11h	48	Saguache A/P

Finally, the wind angle, z_0, and density m parameters were given an offset of 2km, 90°, and $3\frac{\text{kg}}{m^2}$ respectively. These parameters were chosen as they have the most significant effect on the composition on wildfire smoke plume composition [15], and were given an offset to ensure that the algorithm will eventually converge parameters to the original values.

3.2. Error Optimization

Each smoke plume incident was simulated for 20 iterations (at a timeout of $2h$) and for each iteration, the objective function S was re-evaluated against a singular camera. To calculate the partial derivatives as described in Equation 34, the study employed 15 parallel CPUs for $75variables$. After calculating the error for each iteration, a score as shown in Figure 2 was calculated. As seen in Figure 4, for the Mosquito, Electra, and Oak fires, where the most camera information was concentrated, Levenberg-Marquardt managed to reduce the error up to 10-23 times.

However, for 4 other incidents, the cameras were unable to reduce the value of the error. In addition, the error for some cameras converged in fewer iterations and at a much faster rate than the others. There are two primary reasons for an inability to reduce error efficiently: the camera isn't able to view the wildfire or the wildfire is too small. As seen in Figure 3, given that the R value of the linear regression between the amount of area taken up by the segmentation relative to the resolution of the screen and the ability for Levenberg-Marquardt to optimize smoke plume parameters is $R = -0.829$, a failure to view a smoke plume at a sufficient size explains the failure of photogrammetry-based methods. In other words, relative to the resolution of the image, the space took up by the smoke plume was too small to evaluate. Similarly, the size of the wildfire, the distance from said wildfires, and the area burned seem to have no effect on the efficiency of the algorithm, with all of them having R values not exceeding ± 0.2.

Since the position of a pixel and thus the projected size of the smoke plume are functions of the three factors - emission location (and thus, size), position and zoom (Equation 30) - note that none of the factors alone can determine the efficacy of Levenberg-Marquardt. In other words, with a camera with sufficient zoom, a smoke plume can be optimized with the aforementioned methodology.

Another reason for a lack in covergence for certain cameras shown in 3 is due to the fact that when a partial derivative that composes the Jacobian - shown in Equation 34 - is calculated, given that S is small, $J_{i,j} \approx 0$, giving $\kappa_i \approx 0$. The aforementioned result also explains the different convergence rates as shown in Figure 4; given a smaller domain of S (i.e. a smaller smoke plume relative to the resolution), $J_{i,j} = \frac{\partial S}{\partial}$ will also be small, reducing

the size of κ_i. Therefore, for optimal use of the proposed methodology, the smoke plume should ideally cover at least half of the screen or more.

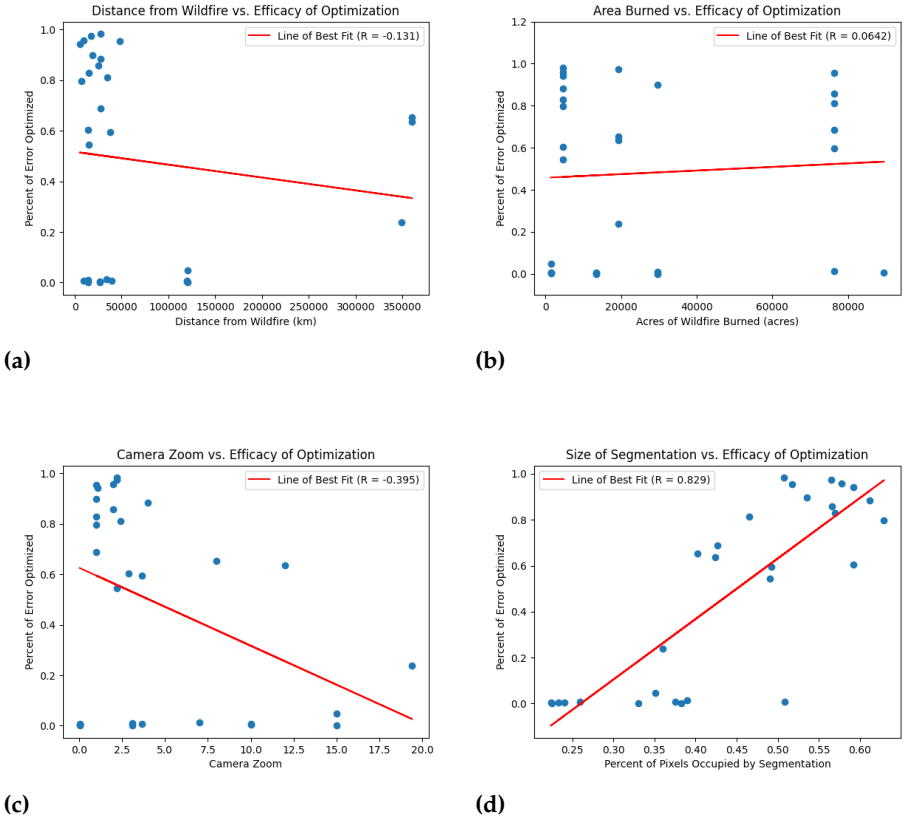

Figure 3. In subfigures (a)-(d), different factors are taken into account to try and explain an inability for gradient descent to optimize for wildfire parameters. As seen above, distance from the wildfire, zoom, and size of the wildfire have no correlation with the ability of Levenberg-Marquardt to reach a local minimum.

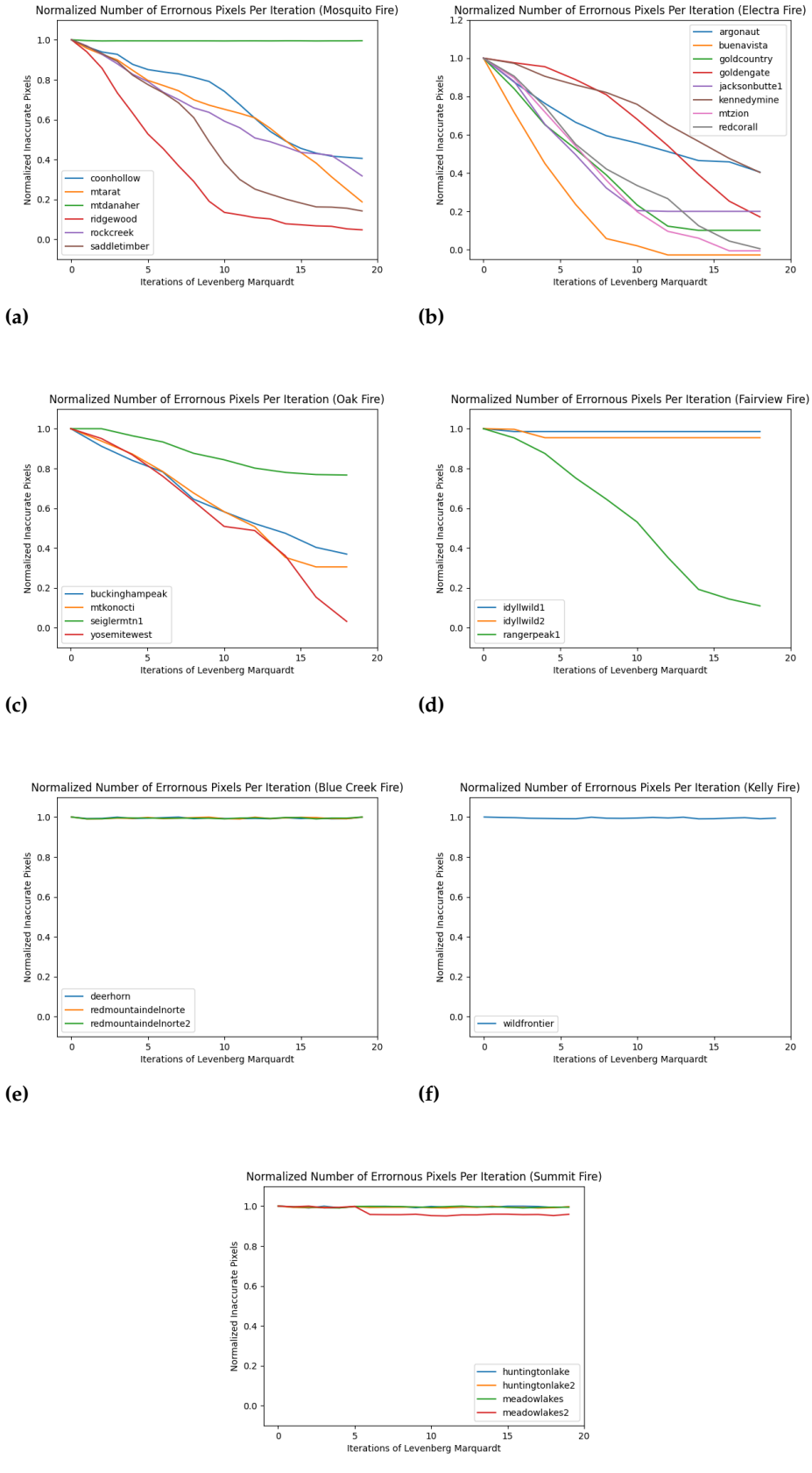

Figure 4. Figures (a)-(g) display optimizations for each fire; as shown in the Figure, in only 20 iterations of the Levenberg-Marquardt algorithm, we were able to reduce the error up to 20x for certain wildfires. However, about half the optimizations did not result in a significantly lower error.

3.2.1. Parameter Evaluation

The three incidents of interest - the Mosquito, Electra, and Oak Fires - are now studied here to evaluate how close they approximate the hidden, correct parameters from an initial, modified parameter in order to ensure correctness of the optimization. These three incidents were chosen as they each had multiple cameras that managed to reduce significantly in error. As seen in Figure 5, each camera managed to converge onto the wind parameter in a few iterations. However, note that the wind angle was not able to converge precisely on the actual value. This is because at far distances, smoke plume composition isn't affected by small changes ($< 10°$) in wind angle.

An advantage of optimizing wind parameters is not only increase in accuracy, but also an availability of more granular metereological information nearby the wildfire. As a comparison, note the wind vectors on the ground layer of the Oak Fire in Figure 6. While the wind parameters were initialized at 100°, after 10 iterations, the wind was not only reverted to 90°, but different intensities of wind at different points of the discretized grid were also measured. Given the computational restrictions of the current study, such a potential increase in metereological granularity not only provides greater smoke plume reconstruction capabilities, but allows greater accuracy in other metereological performances that rely on wind.

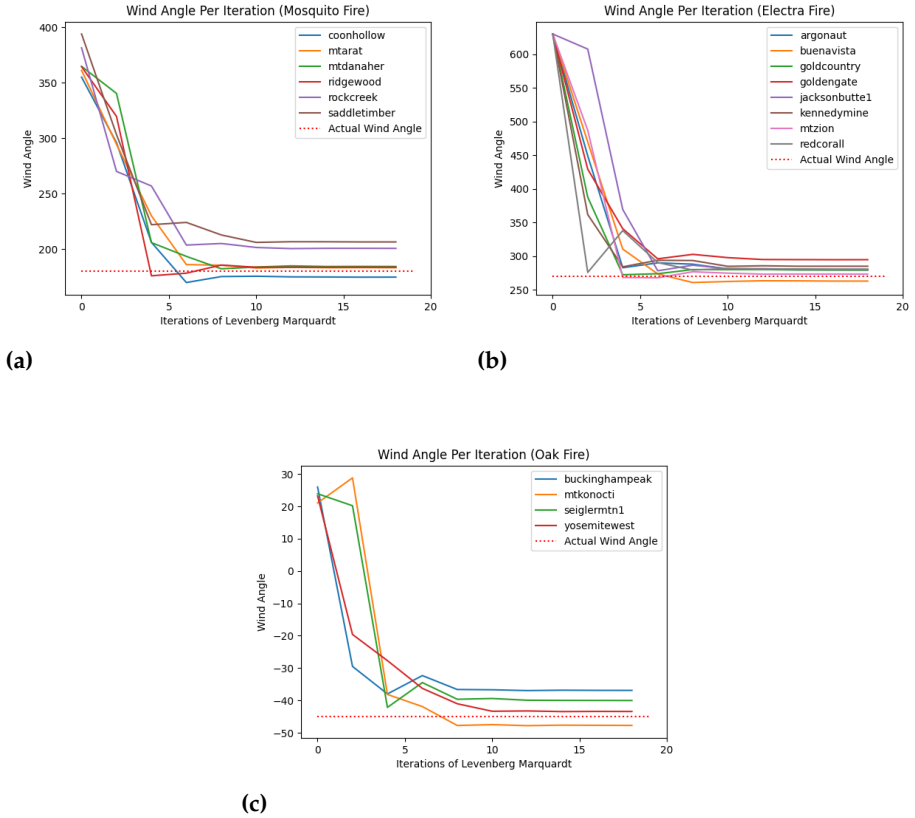

Figure 5. In subfigures (a)-(c), in each iteration, the average wind direction was recorded and are plotted on the graph. The dotted line in each graph represents the actual wind angle, while the solid line shows the predicted wind angles based on the observed iamgery.

A similar evaluation for z_0, the point of temperature gradient inversion, was also conducted. As seen in Figure 7, based on an initial, erroneous inversion point, Levenberg-Marquardt was able to converge onto the correct elevation. However, a weakness with this algorithm was exposed with the elevation convergence for the Mosquito fire; while z_0 was starting to converge to 18 km on iteration 10, z_0 suddenly increased back to its

original value. (cite) If a Levenberg-Marquardt - or another gradient descent algorithm - were to terminate early, the final parameters for the smoke plume could be erroneous. Since such erroneous values are eventually resolved by iteration 20, we recommend to run the gradient-descent algorithm for at least $15 - 20$ iterations.

Finally, a similar procedure was conducted on the density of fuel, where each cell was optimized with NNMF. Surprisingly, the mass of the fuel had no effect on the apparent visual appearance of the smoke plume, as seen in Figure 8, where any apparent changes to fuel density didn't result in the change of error. A potential reason for this is that the emission rate of a smoke plume does not drastically affect S. The proposed algorithm does not account for transparency of the smoke plume; while a greater emission rate would result in a much more opaque smoke plume, the manual segmentation does not make such a distinction.

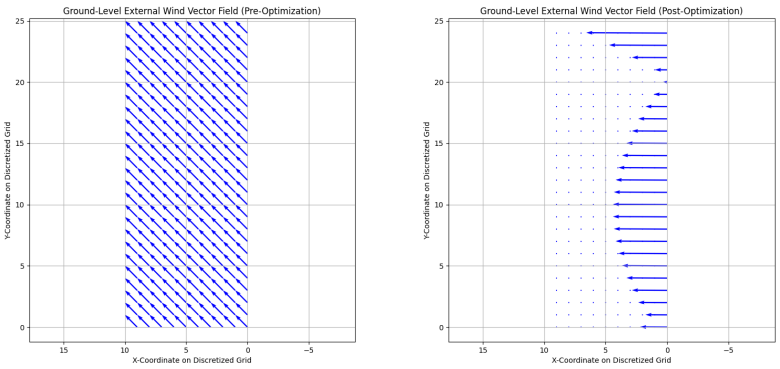

(a) **(b)**

Figure 6. Subfigure (a) shows the wind vectors at ground level before optimization, while Subfigure (b) shows the vectors after optimization with Levenberg-Marquardt.

An example of a smoke plume being optimized is shown in Figure 9; as seen, the smoke plume is first initialized with parameters such that it does not approximate the image as shown. However, after 20 iterations, as seen, the smoke plume starts to come closer to what is seen in the image. Note that there still exists slight error between the observed imagery and the predicted model: the physical simulation has an anvil-like formation on the top of the pyrocumulus cloud, whereas the observed imagery does not. Although a slight error that occured due to a slight underestimation of z_0, it still shows that the accuracy of the physical simulations leave room for improvement with more iterations of Levenberg-Marquardt.

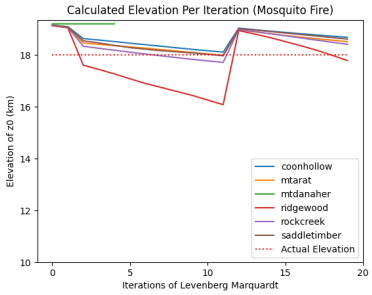

(a)

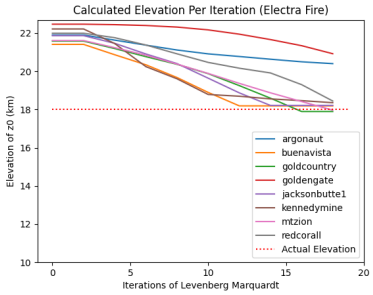

(b)

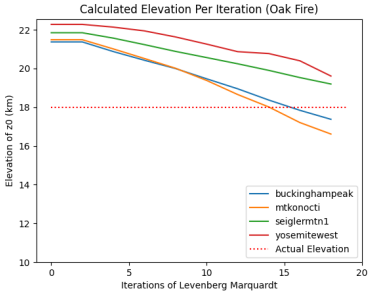

(c)

Figure 7. In subfigures (a)-(c), in each iteration, the average wind direction was recorded and are plotted on the graph.

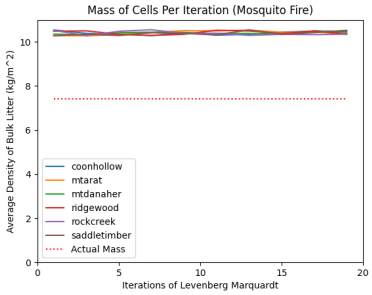

(a)

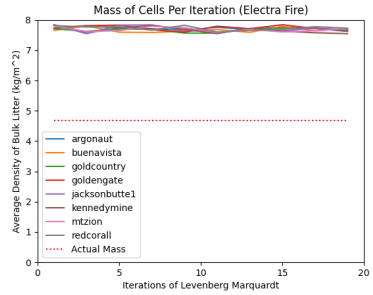

(b)

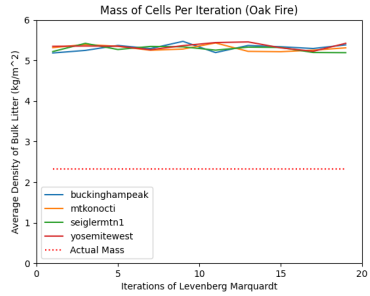

(c)

Figure 8. In subfigures (a)-(c), in each iteration, the average density was recorded and are plotted on the graph.

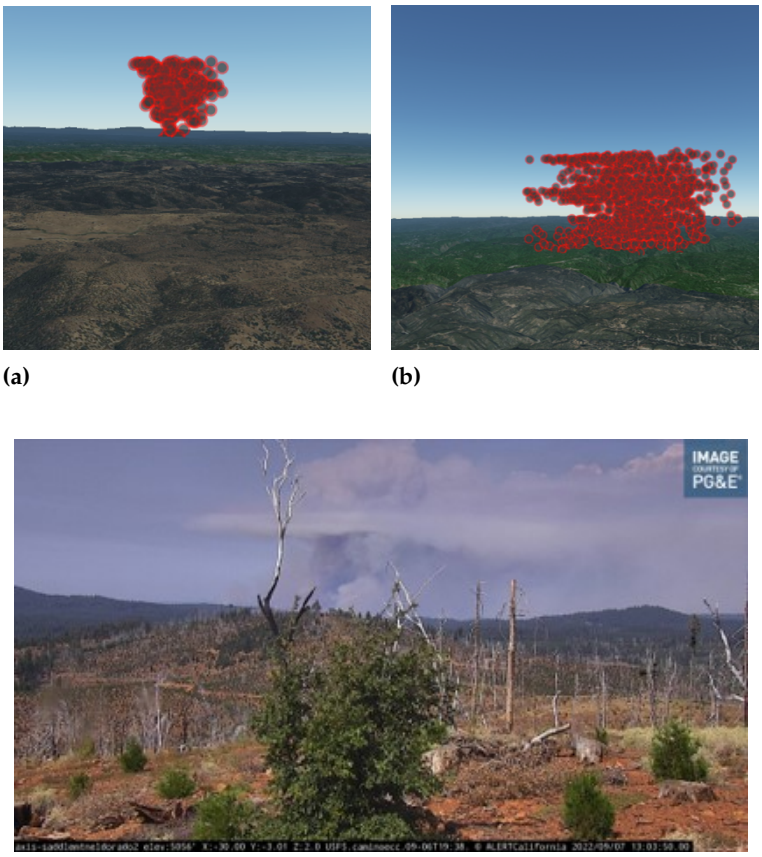

(a) **(b)**

(c)

Figure 9. Subfigure (a) shows the 3D reconstruction of a smoke plume before optimization by Levenberg-Marquardt. Subfigure (b) shows the optimized smoke plume evaluated on the image shown in subfigure (c)

4. Conclusions

This paper proposed a methodology that optimizes smoke plume parameters by comparing it with images. Through tests with a total of 7 wildfires and 21 cameras, this study has established that

1. Given a sufficient amount of space taken up by a smoke plume, Levenberg-Marquardt can reduce the error between the observed imagery and predicted physical simulation. Such efficiency isn't related to the zoom or position of the camera, or even the size of the fire, but rather, the area of the smoke plume captured in the image.
2. Levenberg-Marquardt, in conjunction with imagery, can provide a more granular output on wind and weather parameters, as seen by the ability of the Levenberg-Marquardt algorithm to be able to optimize both f_{ext} and z_0 given a huge error.

Author Contributions: Stephen Guerin, Kasra Manavi, Joshua Thorp, Jaime Gould, and Stephen Graydon: conceptualization, supervision, funding; Gene Huntley: methodology, data analysis, writing, data collection

Funding: SimTable provided camera data from its archive of ALERTCalifornia for research. In addition, SimTable provided funding for conference and paper submissions. Finally, they provided access to standup opportunities for research and paper feedback.

Data Availability Statement: Data will be made available on request.

Acknowledgments: We would like to extend our gratitude to the SimTable team for providing the data required for the research and advice needed for constructing the methodology. In addition, we would like to extend our gratitude to Dr. Cole Monical for his advice in the gathering and analysis of

data. Finally, we would like to extend our gratitude to Ms. Ashli Knoell and Donald Liveoak for the review of this paper.

Conflicts of Interest: The authors declare no conflict of interest.

Appendix A Algorithm to Optimize Per Camera

Algorithm A1 Optimization Algorithm

Data: $z_0, w, \beta_A, \beta_K, f_{ext}, T', m_0, \sigma, \delta, I$
Result: $Q_s \cup Q_c$
$Q_r, Q_c, Q_v, Q_s \leftarrow$ [],[],[],[]
$q_r, q_c, q_v, q_s \leftarrow$ [[[0, 0, ...], ...], ...],[[[0, 0, ...], ...], ...],[[[0, 0, ...], ...], ...],[[[0, 0, ...], ...], ...]
$\lambda \leftarrow 0.1$
$u \leftarrow [[[[0,0,0],...],...],...]$
preverror $\leftarrow \infty$
for *step* $\leftarrow$ 0 **to** 20 **do**
  for $i \leftarrow$ 0 **to** *10* **do**
    $m \leftarrow m - \text{getmass}(\delta, \sigma, q_v)$; // (Eqn 2)
    $u \leftarrow \text{updatewind}(u)$; // (Eqn 20)
    $u \leftarrow \text{incompressibility}(u)$; // (Eqn 21)
    $Q_r, Q_v, Q_c, q_r, q_v, q_c \leftarrow \text{kessler}(q_r, q_v, q_c, Q_r, Q_v, Q_c)$; // (Eqn 12 - 18)
    $T \leftarrow \text{temp}(dm, u)$; // (Eqn 11)
    $B \leftarrow \text{buoyancy}(m, T)$; // (Eqn 22)
    $u \leftarrow u + f_{ext} + B$
    $q_v, q_r, q_c, q_s \leftarrow \text{advect}(q_v, q_r, q_c, q_s, u)$
    $Q_v, Q_r, Q_c, Q_s \leftarrow \text{convert}(q_v, q_s, q_c, q_s)$
  end
  $Q_s, Q_r, Q_c, Q_v \leftarrow \dot{Q}_s, \dot{Q}_r, \dot{Q}_v, \dot{Q}_c$; // (Eqn 30)
  $f''_{ext,x}, f''_{ext,y}, f''_{ext,z}, m'' \leftarrow \text{factor}(f_{ext,x}, f_{ext,y}, f_{ext,z}, m)$; // (Eqn 33)
  $J \leftarrow \text{jacobian}(\{z_0, T'\} \cup f''_{ext,x} \cup f''_{ext,y} \cup f''_{ext,z} \cup m'')$; // (Eqn 34)
  error $\leftarrow S(Q_c \cup Q_s, \Omega_I)$; // (Eqn 31)
  $\kappa \leftarrow \text{step}(J,)$; // (Eqn 35)
  if *error* $<$ *preverror* **then**
    $z_0, T', f''_{ext,x}, f''_{ext,y}, f''_{ext,z}, m'' \leftarrow z_0 + \kappa[0], T' + \kappa[1], f''_{ext,x} + \kappa[2 : |f''_{ext,x}| + 2], + f''_{ext,y} + \kappa[|f''_{ext,y}| + 2 : |f''_{ext,x}| + 2 + |f''_{ext,y}|], f''_{ext,z} + \kappa[f''_{ext,x}| + 2 + |f''_{ext,y}| : -|m''|], m'' + \kappa[-|m''| :]$
    preverror $\leftarrow$ error
    $\lambda \leftarrow \lambda * 2$
  else
    $\lambda \leftarrow \lambda / 3$
  end
end

References

1. McKenzie, D.; Geadoff, Z.; Peterson, D.L.; Mote, P. Climatic change, Wildfire, and conservation *Consv. Biology* **2004**, *18*, 890—902.
2. Haikerwal, A.; Akram, M.; Del Monaco, A.; Smith, K.; Sim, M.; Meyer M.; Tonkin, A.M.; Abramson, M.J.; Dennekamp, M. Impact of fine particulate matter (PM 2.5) exposure during wildfires on cardiovascular health outcomes In *Journal for AAA* **2015**, *7*.
3. Xiao W.; Erik S.; Michael D.M; Michael W.W; Stefan W. Low-intensity fires mitigate the risk of high-intensity wildfires in California's forests In *Science Advances* **2023**, *9*.
4. Dennekamp M, Abramson MJ. 2011. The effects of bushfire smoke on respiratory health. Respirology 16:198-209; https://doi.org/10.1111/j.1440-1843.2010.01868.x https://pubmed.ncbi.nlm.nih.gov/20920143/
5. Lee TS, Falter K, Meyer P, Mott J, Gwynn C. 2009. Risk factors associated with clinic visits during the 1999 forest fires near the Hoopa Valley Indian Reservation, California, USA. Int J Environ Health Res 19(5):315-327
6. Burke, M., Heft-Neal, S., Li, J. et al. Exposures and behavioural responses to wildfire smoke. Nat Hum Behav 6, 1351–1361 (2022). https://doi.org/10.1038/s41562-022-01396-6

7. Johnston, F. H., Henderson, S. B., Chen, Y., Randerson, J. T., Marlier, M., DeFries, R. S., … Brauer, M. (2012). Estimated global mortality attributable to smoke from landscape fires. Environmental Health Perspectives, 120(5), 695–701. doi:10.1289/ehp.1104422
8. Brey, S. J., Ruminski, M., Atwood, S. A., and Fischer, E. V.: Connecting smoke plumes to sources using Hazard Mapping System (HMS) smoke and fire location data over North America, Atmos. Chem. Phys., 18, 1745–1761, https://doi.org/10.5194/acp-18-1745-2018, 2018.
9. Aguirre, C., Berri, G., Dezzutti, M., Queirel, J. M., Marcos, E., Sedano, C., & Rondán, G. (2022). Atmospheric dispersion simulation of an accidental smoke plume using a heat diffusion algorithm into a les-sto coupled model. Atmospheric Environment: X, 14, 100172. doi:10.1016/j.aeaoa.2022.100172
10. McGrattan, K.B.; Baum, H.R.; Rehm, R.G. 1996. Numerical simulation of smoke plumes from large oil fires. Atmospheric Environment. 30(24):4125-4136.
11. Ferrero, E., Alessandrini, S., Anderson, B., Tomasi, E., Jimenez, P., & Meech, S. (2019). Lagrangian simulation of smoke plume from fire and validation using ground-based lidar and aircraft measurements. Atmospheric Environment, 213, 659–674. doi:10.1016/j.atmosenv.2019.06.049
12. Kumar, A., Pierce, R. B., Ahmadov, R., Pereira, G., Freitas, S., Grell, G., … Guo, H. (2022). Simulating wildfire emissions and plume rise using geostationary satellite fire radiative power measurements: A case study of the 2019 Williams flats fire. Atmospheric Chemistry and Physics, 22(15), 10195–10219. doi:10.5194/acp-22-10195-2022
13. Hädrich, T., Banuti, D. T., Pałubicki, W., Pirk, S., & Michels, D. L. (2021b). Fire in Paradise. ACM Transactions on Graphics, 40(4), 1–15. doi:10.1145/3450626.3459954
14. Kalnay et al.,The NCEP/NCAR 40-year reanalysis project, Bull. Amer. Meteor. Soc., 77, 437-470, 1996
15. Liu, Y., Achtemeier, G. L., Goodrick, S. L., & Jackson, W. A. (2010). Important parameters for smoke plume rise simulation with Daysmoke. Atmospheric Pollution Research, 1(4), 250–259. doi:10.5094/apr.2010.032
16. Hädrich, T., Makowski, M., Pałubicki, W., Banuti, D. T., Pirk, S., & Michels, D. L. (2020a). Stormscapes. ACM Transactions on Graphics, 39(6), 1–16. doi:10.1145/3414685.3417801
17. Ramasubramanian, M., Kaulfus, A., Maskey, M., Ramachandran, R., Gurung, I., Freitag, B., & Christopher, S. (2019). Pixel level smoke detection model with Deep Neural Network. Image and Signal Processing for Remote Sensing XXV, 39. doi:10.1117/12.2532562
18. Larsen, A., Hanigan, I., Reich, B.J. et al. A deep learning approach to identify smoke plumes in satellite imagery in near-real time for health risk communication. J Expo Sci Environ Epidemiol 31, 170–176 (2021). https://doi.org/10.1038/s41370-020-0246-y
19. Zhao, L., Liu, J., Peters, S., Li, J., Oliver, S., & Mueller, N. (2022). Investigating the Impact of Using IR Bands on Early Fire Smoke Detection from Landsat Imagery with a Lightweight CNN Model. Remote Sensing, 14(13), 3047. https://doi.org/10.3390/rs14133047
20. Kim, H. C., Chai, T., Stein, A., and Kondragunta, S.: Inverse modeling of fire emissions constrained by smoke plume transport using HYSPLIT dispersion model and geostationary satellite observations, Atmos. Chem. Phys., 20, 10259–10277, https://doi.org/10.5194/acp-20-10259-2020, 2020.
21. Xie, Y., Qu, J. J., Xiong, X., Hao, X., Che, N., & Sommers, W. (2007). Smoke plume detection in the Eastern United States using Modis. International Journal of Remote Sensing, 28(10), 2367–2374. doi:10.1080/01431160701236795
22. Saghri, J., Jacobs, J., Kohler, D., Davenport, T., & Moussa, G. (2012). Characterization and identification of smoke plume for early forest fire detection. SPIE Proceedings, 8499. doi:10.1117/12.930755
23. "Internet, smartphone and social media use." Pew Research Center, Washington, D.C. (2022) https://www.pewresearch.org/global/2022/12/smartphone-and-social-media-use-in-advanced-economies-2022/.
24. Alertcalifornia. (2024). Retrieved from https://alertcalifornia.org/
25. Andrews, P. L. (2018). The Rothermel Surface Fire Spread Model and Associated Developments: A Comprehensive Explanation. doi:10.2737/rmrs-gtr-371
26. Tory, K. J., & Thurston, W. (2015). Pyrocumulonimbus: A literature review. Bushfire and Natural Hazards CRC: East Melbourne, VIC, Australia.
27. E. Kessler. 1969. On the Distribution and Continuity of Water Substance in Atmospheric Circulations. American Meteorological Society, Boston, MA, 1–84.
28. Abdulkadirov R, Lyakhov P. Estimates of Mild Solutions of Navier–Stokes Equations in Weak Herz-Type Besov–Morrey Spaces. Mathematics. 2022; 10(5):680. https://doi.org/10.3390/math10050680
29. Moré, J. J. (1978). The Levenberg-Marquardt Algorithm: Implementation and theory. Lecture Notes in Mathematics, 105–116. doi:10.1007/bfb0067700
30. The weather year round anywhere on Earth. (n.d.). Retrieved from https://weatherspark.com/
31. Aerial Information Systems, Inc. (2015). Western Riverside County Vegetation Mapping Update.
32. Wildfire progressions list. (n.d.). Retrieved from https://simtable.com/apps/fireProgression/output2024/index.html